

Progress of International Program on Hydrogen Production with the Copper-Chlorine Cycle

G. F. Naterer^{1*}, S. Suppiah², L. Stolberg³, M. Lewis⁴, S. Ahmed⁵, Z. Wang⁶, M. A. Rosen⁷, I. Dincer⁸,
K. Gabriel⁹, E. Secnik¹⁰, E. B. Easton¹¹, S. Lvov¹², V. Papangelakis¹³, A. Odukoya¹⁴

^{1, 14} Memorial University of Newfoundland, St. John's, Newfoundland, Canada

^{2, 3} Atomic Energy of Canada Limited (AECL), Chalk River, Ontario, Canada

^{4, 5} Argonne National Laboratory, Argonne, Illinois, U.S.

⁶⁻¹¹ University of Ontario Institute of Technology (UOIT), Oshawa, Ontario, Canada

¹² Pennsylvania State University, University Park, Pennsylvania, U.S.

¹³ University of Toronto, Toronto, Ontario, Canada

Abstract

This paper highlights the recent advances in thermochemical hydrogen production with the copper-chlorine (Cu-Cl) cycle. Extended operation and performance of HCl/CuCl electrolysis is presented. Advances in the development of improved electrodes are presented for various electrode materials. Experimental studies for a 300 cm² electrolytic cell show a stable current density and production at 98% of the theoretical hydrogen production rate. Long term testing of the

^{1*} Corresponding Author: Professor and Dean, Faculty of Engineering and Applied Science, Memorial University of Newfoundland, St. John's, NL, A1B 3X5, Email: gnaterer@mun.ca; Phone: (709) 864-8864, Fax: (709) 864-8975

² Manager, Hydrogen Isotopes Technology Branch, AECL, Chalk River, Ontario, Canada, K0J 1J0

³ Scientist, Hydrogen Isotopes Technology Branch, AECL, Chalk River, Ontario, Canada, K0J 1J0

⁴ Chemist, Chemical Engineering Division, Argonne National Laboratory, 9700 S. Cass Ave., Argonne, IL, 60439

⁵ Chemical Engineer, Chemical Engineering Division, Argonne National Laboratory, 9700 S. Cass Avenue, Argonne, Illinois, USA, 60439

⁶ Hydrogen Program Director, UOIT, 2000 Simcoe Street North, Oshawa, Ontario, Canada, L1H 7K4

⁷ Professor of Mechanical Engineering, UOIT, 2000 Simcoe Street North, Oshawa, Ontario, Canada, L1H 7K4

⁸ Professor of Mechanical Engineering, UOIT, 2000 Simcoe Street North, Oshawa, Ontario, Canada, L1H 7K4

⁹ Professor of Mechanical Engineering, UOIT, 2000 Simcoe Street North, Oshawa, Ontario, Canada, L1H 7K4

¹⁰ Research Laboratory Manager, Faculty of Engineering and Applied Science, UOIT, 2000 Simcoe Street North, Oshawa, Ontario, Canada, L1H 7K

¹¹ Associate Professor of Chemistry, UOIT, 2000 Simcoe Street North, Oshawa, Ontario, Canada, L1H 7K42

¹² Professor of Energy and Mineral Engineering, Department of Materials Science and Engineering, Pennsylvania State University, 207 Hosler Building, University Park, PA 16802

¹³ Professor of Chemical Engineering, University of Toronto, 200 College Street, Toronto, Ontario, M5S 3E5

¹⁴ Research Engineer, Faculty of Engineering and Applied Science, Memorial University of Newfoundland, St. John's, Newfoundland, A1B 3X5

electrolyzer for 1,000 h also shows a stable cell voltage. Different systems to address integration challenges are also examined for the integration of electrolysis/hydrolysis and thermolysis/electrolysis processes. New results from experiments for CuCl-HCl-H₂O and CuCl₂-HCl-H₂O ternary systems are presented along with solubility data for CuCl in HCl-H₂O mixtures between 298 and 363 K. A parametric study of multi-generation energy systems incorporating the Cu-Cl cycle is presented with an overall energy efficiency as high as 57% and exergy efficiency of hydrogen production up to 90%.

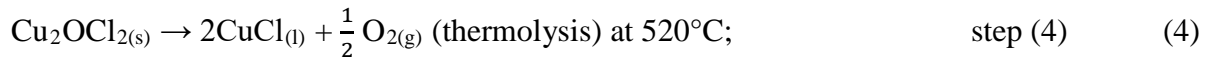
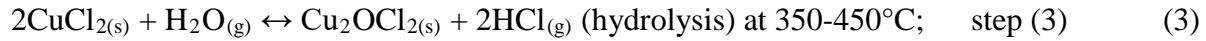
1. Introduction

Utilization of hydrogen as a clean energy carrier is a promising alternative to conventional fossil fuels. Sustainable, lower cost, and “green” methods of hydrogen production are needed to adopt hydrogen on a wider scale. Usage of hydrogen has the potential to significantly reduce the emissions of greenhouse gases that contribute to climate change, if produced using renewable energy sources. This is one of the reasons why hydrogen is often cited as a future energy carrier that can become a significant contributing factor to sustainable energy supply [1], as well as a prominent fuel.

Large-scale sustainable methods of hydrogen production require an energy source such as nuclear or solar energy. For large-scale capacities of hydrogen production, thermal energy can be supplied by nuclear reactors. Electrolysis is a commercially available technology that uses electricity for water splitting and hydrogen production. Thermochemical cycles are promising water splitting alternatives that can be linked with nuclear reactors to thermally decompose water

into oxygen and hydrogen, through a series of intermediate reactions. The Cu-Cl cycle is a hybrid thermochemical cycle, including both electrochemical and thermal steps. This paper outlines recent advances in thermochemical hydrogen production with the Cu-Cl cycle.

The copper-chlorine Cu-Cl cycle is a promising cycle for hydrogen production by thermochemical water decomposition due to its lower temperature requirement and better overall efficiency than other thermochemical cycles [2-4]. The Cu-Cl cycle consists of a closed loop of thermally driven chemical reactions, where water is decomposed into hydrogen and oxygen, and all other intermediate compounds are recycled with no emissions to the environment [2,3,5]. This paper focuses on the four step Cu-Cl cycle for hydrogen production as described in Fig. 1. The four reactions of the Cu-Cl cycle are:



In comparison to other thermochemical cycles, the Cu-Cl cycle has the advantage of an ability to utilize low-grade waste or process heat to achieve higher thermal efficiency and lower cost of hydrogen production than other technologies [6-8]. The Cu-Cl cycle has a reduced electrical power requirement, compared to typical water electrolysis, for its CuCl/HCl electrolysis. The CuCl₂ hydrolysis reaction and Cu₂OCl₂ thermolysis reaction form a closed loop with the CuCl/HCl electrolyzer to produce hydrogen in the cycle. In the hydrolysis reactor, the chemical

conversion effectiveness decreases as reactants are consumed [9]. Past studies on the conversion extent of the solid hydrolysis reactant indicated an optimal conversion of 4 mol to 15 mol of steam per mol of HCl produced [10]. Experimental data [11] and thermodynamic analysis [12,13] suggest an optimal temperature of the hydrolysis reactor to be approximately 375 °C. Lewis et al. [14] examined the conversion extent in the CuCl/HCl electrolyzer. In the Cu₂OCl₂ thermolysis reactor, a conversion extent of 85 % was reported [14]. In this paper, the integration of the electrolyzer and hydrolysis reactor in the Cu-Cl cycle is reported in terms of energy and mass flows. A crystallization process is also reported to reduce the quantity of H₂O entering the hydrolysis reactor.

Past studies have successfully demonstrated the unit operations of each of the processes of the Cu-Cl cycle [15,16]. Few studies have examined the integration of reactions and interaction between processes. The hydrolysis process and its integration with electrolysis entail significant challenges. These include the excess steam requirement of the hydrolysis reaction above the stoichiometric amount to obtain >95 % yield of Cu₂OCl₂. The concentration of the produced HCl in the hydrolysis reaction is not sufficient to meet the minimum requirement of the electrolysis reaction. Increasing the steam to CuCl₂ ratio only further reduces the concentration of HCl. The operating temperature of the hydrolysis and electrolysis reactions differs significantly, requiring a substantial heat exchange to condense the high temperature effluent and reheat the products for subsequent processes in the cycle [10,15,17].

Recent results of analysis of the integration of the hydrolysis and electrolysis steps were reported by Sayeed et al. [16]. Results of the kinetics in the hydrolysis reactor indicate that excess steam is required in the hydrolysis reactor, which subsequently reduces the overall efficiency of the Cu-Cl cycle. The adverse effects of excess steam on the cycle efficiency were reduced by using a heat recovery steam generator (HRSG) to provide the excess steam required in the reaction. The results showed that steam produced in the HRSG is about 14 times higher than that observed from the stoichiometric reaction.

The paper presents recent advances toward an integrated thermochemical Cu-Cl cycle. Individual unit operations have been developed, built and tested in combination with subsequent intermediate processes. Research and development is also reported for corrosion-resistant materials for use in the reactors, membrane development, electrode development, and crystallization studies. Results are presented and discussed for a number of case studies. The paper describes recent progress of a Canadian-led international team, including a number of institutions from Canada, U.S., Slovenia, Romania and Argentina, towards industrialization of the Cu-Cl cycle, and extends previous reports of progress by the team [3, 16, 17, 21].

2. Thermochemical Copper-Chlorine (Cu-Cl) Cycle

Figure 1 depicts a schematic representation of the four step Cu-Cl cycle for hydrogen production. There are different variations of the Cu-Cl cycle, consisting of 3 to 5 main reactions which yield a net reaction that decomposes water into hydrogen and oxygen [14]. In this paper, the main focus is the 4-step cycle since separation of hydrolysis and drying processes provides key

advantages of higher thermal efficiency and more viable practical adaptation [18]. The overall thermal efficiency of the Cu-Cl cycle has been estimated to be approximately 40-43% [10,19] based on the lower heating value (LHV) of hydrogen.

In the oxygen production step of the Cu-Cl cycle (step 4), an intermediate compound, solid copper oxychloride (Cu_2OCl_2), is decomposed into oxygen gas and molten cuprous chloride (CuCl). The solid feed of Cu_2OCl_2 is supplied to the oxygen production reactor from the CuCl_2 hydrolysis reaction (step 3) that operates at a temperature of 350–450 °C. Gas species leaving the oxygen reactor include oxygen gas and potentially impurities of products from side reactions, such as CuCl vapor, chlorine gas, HCl gas (trace amount) and H_2O vapour (trace amount). The substances exiting the reactor are molten CuCl, potentially solid CuCl_2 from the upstream hydrolysis reaction, due to the incomplete decomposition of CuCl_2 at a temperature lower than 550 °C [20], as well as reactant particles entrained by the flow of molten CuCl.

3. CuCl/HCl Electrolysis

Atomic Energy of Canada Limited (AECL), Gas Technology Institute (GTI) and Pennsylvania State University (PSU) are developing the CuCl/HCl electrolyzer. Work is focused on this step because preliminary process design and economic analysis show that the major cost and energy drivers are the electrolyzer and its components [21,22]. Early experimental studies also showed that catastrophic failure of the electrolyzer could occur under some operating conditions. Research is currently focused on the determination of the optimum design and operating conditions, such as membrane type, catalyst loading, temperature and pressure, anolyte

and catholyte compositions, and flow rate. The goal is to meet cost and energy usage targets for producing 1-10 kg of H₂/day by achieving long lifetimes and lower costs of the catalyst and membrane while maximizing current density at the desired cell potential. In the short term (2015), hydrogen produced at less the \$6/kg H₂ by the Cu-Cl cycle would be commercially competitive. The long term target (2025) for commercial hydrogen production is a cost of \$4/kg H₂. Table 1 presents a summary of ongoing work at AECL, GTI and PSU and some of the conditions of their tests.

Scale-up. Testing of the one 300 cm² cell showed a current density of 0.55 A/cm² at 0.7 V. A two 300 cm² cell stack was then fabricated and tested to ensure that the mass flow distribution was even and that there were no shunt currents. At 0.7 V, the current density was 0.36 A/cm² and H₂ production was 98% of the theoretical value. Conversion of Cu(I) to Cu(II) was 65% when the flow rate was 210 mL/min.

Preliminary tests with the five-cell stack showed a large drop off in current within 20 minutes of the start of the test, indicating much of the Cu(I) was consumed. Two major changes in the ancillary equipment were therefore necessary - a higher capacity pump to provide greater flow rates and a redesigned recycle system with a larger capacity. An optimized flow rate will improve the reactant mass transfer uniformity to obtain maximum performance. The optimized flow rate for the single cell and five cell tests are 250 ml/min and 1 liter/min, respectively. After these changes, the polarization curves for the 5 cells overlapped each other as shown in Fig. 2 but the current density was low at 0.15 A/cm², suggesting insufficient Cu(I). Subsequent tests that

included a longer recycle time and an increase in cathode flow rate from 600 to 800 mL/min showed higher current densities, 0.15 A/cm² and 0.19 A/cm², respectively. Tests with various flow rates at PSU confirmed the importance of flow rate. GTI is also studying the use of the CG2 membrane in 300 cm² cells.

Effect of increasing temperature. Details of the chemistry, the electrolyzer system and changes made to accommodate operation at 100 °C are described elsewhere [23]. The results of the tests at 40-100 °C are shown in Fig. 3. At 0.7 V, there was a 15 % increase in current density as the temperature was increased from 80 to 100 °C. Electrochemical Impedance Spectroscopy (EIS) measurements showed that the increase in current density was due to decreases in internal ohmic and charge transfer resistances [24].

Lifetime tests. The results of the 168 hour lifetime test at 80 °C are shown in Fig. 4. The time period (168 hours) is based on limitations of the current experimental setup. The current density decreased from an initial value near 0.5 A/cm² to about 0.3 A/cm² (the milestone values) at the end of the test. The cell was operational for 168 hours while the membrane was contacted by the solution for over 400 hours. The hydrogen production rate was measured and found to be ≥95 % of the theoretical value predicted by Faraday's Law. EIS was used to characterize the electrolyzer processes. Analysis of the EIS data is ongoing but preliminary results indicated that the internal ohmic resistance increased with time, which suggests membrane degradation.

Pt loading studies. SEM images of electrode surfaces indicated that Pt loading techniques previously used in the CuCl/HCl electrolytic cell resulted in a dense deposit, suggesting that at

least some of the Pt was inactive [25] . A dense deposit provides a smaller surface area for the electrochemical reaction, possibly covering Pt by carbon, which may render some Pt particles inactive. To obtain a thinner deposit, the catalyst ink was applied via an airbrush. SEM images shown in Fig. 5 show differences in the Pt surfaces with painting and airbrushing. When the airbrushed Pt loadings were reduced to 0.1 and 0.4 mg/cm² on the anode and cathode, respectively, the current density was 0.55 A/cm², which was similar to that achieved when the Pt loading was 0.8 mg/cm² on each electrode.

Atomic Energy of Canada Limited (AECL) has been carrying out long term performance tests to determine the long term stability of the cell voltage at a constant current density of 0.1 A/cm². For these tests the electrode area was reduced to 5 cm². AECL's results show that the electrolyzer can operate over a long period and display stable cell voltage performance, as seen in Fig. 6 for more than 1,000 h of operation. The conditions used to study the long term performance of the AECL electrolyzer are summarized in Table 2. During shutdown periods, the electrolytes are still circulated through the cell. Thus, the voltage is different after each restart. During the shutdown period, all of the copper (II) in the system will have been converted back to copper (I). Also, the hydrogen present in the catholyte is purged out of the catholyte during the shutdown period. These two changes will affect the equilibrium potential of the cell. These transient periods may occur as a result of chemistry changes that occur within the system during shutdown. It is important to notice that eventually the system is able to return to a cell voltage although noisy at steady state. The noise is not always observed during experimentation, which indicates further

investigation is required. Throughout the experiment, a drop in the catholyte HCl concentration is observed.

Another major objective in the development of the CuCl/HCl electrolyzer is to suppress copper species crossover from the anolyte to the catholyte during CuCl/HCl electrolysis. Two approaches have been adopted. The first approach is to develop membranes that can suppress copper species crossover while the second approach is more focused on the design of the electrolyzer itself. Both approaches together have allowed a significant reduction in the amount of copper species that cross over and enter the catholyte during CuCl/HCl electrolysis. Another achievement to report has been the in-situ measurement of the various components that define the cell voltage during a long term test. The change in cell voltage with time is measured in-situ and it is periodically interrupted to measure the cell impedance. This allows the ohmic resistance of the cell to be estimated at a high frequency, where the imaginary impedance is zero. The polarization curves are also measured in-situ to determine the equilibrium potential and the activation overpotential. The ohmic resistance and the activation overpotential are used to calculate the cell voltage, which are compared to the experimentally determined data. These measurements show that the electrolyzer resistance needs to be reduced in order to improve the cell voltage performance.

Studies of copper (I) diffusion through the membrane of the electrolyzer were also investigated. Copper (I) was maintained as copper (I) by circulating the anolyte through three columns containing copper metal – the diffusing copper (I) species was CuCl_4^{3-} in 11 M HCl and

CuCl_3^{2-} in 6 M HCl. The catholyte copper concentrations were determined using UV-visible spectrophotometry. The results from the experiments showed a linear dependence of the catholyte copper concentration on operation time. The linear relationship was valid up to a catholyte concentration of ~300 mg/L. The experimental results were used to determine the diffusion coefficient, which was found to be $5 \times 10^9 \text{ cm}^2/\text{s}$. The results showed that copper (I), an anionic copper species, can diffuse through a cation exchange membrane. Since during electrolysis an electric field is present between the electrodes, one would expect that the movement of copper (I) through the membrane would be limited as the field would oppose the negative charge on the anionic copper (I) species. However, copper (I) was still found to pass through the membrane but at a somewhat lower rate. This suggests that the driving force for diffusion is greater than the driving force for migration under the experimental conditions of electric field present during the test. In 6 M HCl the diffusion of copper (I) in the absence of an electric field was a factor of 4 higher than what was observed when 11 M HCl was studied.

A HYSYS economic model of the fully integrated Cu-Cl cycle is being developed. The model will be optimized for economical hydrogen production by identifying the optimal cell operating conditions. A performance model of the electrolyzer will also be developed and analyzed with COMSOL.

4. Thermolysis Process

The oxygen decomposition reactor is the highest energy consuming device in the Cu-Cl cycle. The thermolysis process occurs at 530 °C in the reactor and it is the highest temperature

required in the cycle. Scaling up this process is essential in developing an integrated pilot plant of the Cu-Cl cycle. The volume of oxygen reactor depends on the residence time, which determines the size of the reactor. The residence time of the oxygen reactor is the time required for the solid Cu_2OCl_2 particles to decompose completely into molten CuCl and oxygen gas. It is necessary to validate the residence time experimentally in order to calculate the volume of oxygen reactor. Residence times based on experimental studies have been reported by Rosen et al. [7]. This data is useful for scaling up the oxygen reactor.

The minimum size of the oxygen reactor is the size required by the liquid volume of molten salt without gas bubbles. The direct contact heat transfer from molten CuCl to solid Cu_2OCl_2 (reactant) particles reduces the heat required in the oxygen reactor. The molten bath can be sustained by the exothermic reaction occurring in the reactor. The reactor is initially filled with molten salt and solid particles are later fed continuously into the reactor.

An option for the normal configuration for the process vessel for the oxygen reactor is a vertical cylindrical section closed by dished ends [8]. Several designs are possible [26] but in order to simplify design and minimize costs, standard reactor designs are recommended. When limiting the size of oxygen reactor to a specified volume, the number of reactors can be estimated by $N = V / (D^2 H \pi / 4)$. The aspect ratio AR (ratio of the reactor's height to its diameter, H/D) is selected based on the capital cost, mixing, and heat transfer characteristics of the oxygen reactor. A reasonable compromise of these competing effects is to use an aspect ratio of around 2, which is frequently used for chemical reactors [27].

The wall thickness of the reactor is dependent on reactor diameter, and consideration must be given to manufacturing of the reactor. Transportation of vessels over 4.6 m in diameter is difficult because of standard road bridge dimensions and overhead electric lines [28]. Taking these factors into consideration, the maximum reactor diameter analyzed was 4.2 m. To avoid a very large size reactor, multiple smaller oxygen reactors can be used. Table 3 shows dimensions and numbers of oxygen reactors for different hydrogen production rates and residence times.

5. System Integration of Unit Operations

In this section, the experimental and numerical results of thermolysis/electrolysis integration, hydrolysis/electrolysis integration, solubility, and HCl/Cu-Cl₂ separation processes are presented.

5.1 Crystallization and Solubility of CuCl₂-CuCl-HCl-H₂O System

The experiment on crystallization and solubility of the ternary process has been reported by Wang et al [15]. This paper reports further results from investigations carried out by researchers at UOIT. In Table 4, the crystallization properties of a CuCl₂-CuCl-HCl solution are presented for 1 litre of the solution between 20 °C and 80 °C on the basis that the crystallization process operates on the solubility curve. For each temperature, a solution is selected based on the ratio of CuCl₂-CuCl-HCl in the solution to best match the concentration of the electrolyzer effluent.

The effect of temperature of the solution on the crystallization effectiveness (ζ) is reported in Fig. 7. The amount of solids is determined by the product of crystallization effectiveness and the molar input. As presented in Fig. 7, the crystallization of CuCl is negligible between 80 °C and

60 °C, while 18 % of CuCl₂ is crystallized. Table 4 shows that the HCl concentration is increased from 6.09 to 8.55 M from 80 °C to 60 °C, which may contribute to the relative quantities of CuCl and CuCl₂ solids. As presented in Fig. 8, a significant portion of the energy input to the hydrolysis reactor is used to convert water to steam, particularly when the steam requirement is high. Fig. 8 also highlights the importance of maintaining a low steam requirement in the hydrolysis reactor since higher steam requirements require a significantly higher energy input than the theoretical minimum requirement for water electrolysis, 286 kJ/mol.

As illustrated in Fig. 9, the quantity of H₂O in the electrolyzer effluent rises significantly with a lower conversion extent. An input electrolyte solution of 2 M CuCl and 6 M HCl, and a 50 % conversion in an electrolyzer, will produce an effluent of 1 M CuCl₂ and 42.7 M of H₂O. This increases the minimum hydrolysis input energy to 2,940 kJ/mol of CuCl₂, if the effluent stream is directly fed to the hydrolysis reactor to provide the steam and CuCl₂ reactants. In contrast, utilizing a crystallizer in the temperature range of 80 °C to 60 °C, will result in a loss of 85 kJ/mol into the crystallizer, to produce 0.17 M of CuCl₂ solids. To produce 1 M of CuCl₂ solids will require 502 kJ/mol of thermal energy contained in the solution. This is a comparable value in magnitude to the minimum energy requirement of the hydrolysis reactor with an excess steam requirement of 8 (507 kJ/mol of CuCl₂).

5.2 Integration of Thermolysis and Electrolysis

Experiments were performed to better understand the physics of liquid-solid systems and the dissolution rate of copper chloride (CuCl) in hydrochloric acid (HCl). The first experiment

consists of dropping CuCl(s) into water to analyze the flow dynamics of the particle. The second set of experiments consisted of dropping CuCl(s) particles in HCl(aq) and recording the time required for dissolution. Initially, the particles were dropped in stagnant HCl(aq) and local saturation could be observed. To speed up the dissolution rate and avoid local saturation occurring near the particle surface, nitrogen was injected from the bottom of the container.

The results pertaining to the CuCl (s) particle in quiescent 12 M HCl (aq) are presented in Fig. 10 (a). It is observed that the particle's area decreases linearly as follows:

$$Y = -0.0053X + 9.4377 \quad (5)$$

where Y represents the surface area, and X is time. This representation returned an R-squared value of 0.98505, which indicates a good correlation between the points. The data pertaining to the dissolution rate of CuCl(s) in 12 M HCl(aq) in the presence of nitrogen as the mixing agent has a similar trend as observed in Fig. 10 (b). A linear dissolution rate is observed as follows:

$$Y = -0.0125X + 13.636 \quad (6)$$

This returned an R-squared value of 0.97971, which indicates a good correlation between the points. The results indicate that when nitrogen bubbles are introduced as a mixing agent, the time to dissolve a particle with the same area was reduced by about half.

5.3 Solubility Comparison of Binary and Ternary Systems

The flow that discharges from the anode side of the copper (I) chloride electrolysis process will be a quaternary system of CuCl, CuCl₂, HCl, and H₂O. After leaving the anode, this flow will

be passed to a crystallizer to produce a concentrate of copper (II) chloride, which is recycled in the process. A quaternary solubility model is needed for the design of the cupric chloride concentration process, where it will be used to determine temperature and hydrochloric acid concentration conditions under which cupric chloride can be selectively precipitated from the solution. In the design of the electrolyzer, a quaternary solubility model is required to determine the necessary conditions for equilibrium in the electrolytic reaction.

New solubility data for the CuCl-HCl-H₂O system was produced and covered a hydrochloric acid concentration range of 1 to 12 mol/kg and a temperature range of 298 K to 363 K [35]. A detailed diagram of the apparatus is given in Fig. 11. The studies, which involved withdrawing and analyzing samples at regular intervals until the cuprous chloride concentration remained constant, revealed fast kinetics at room temperature, with equilibrium reached in less than five minutes for all acid concentrations. The copper concentration was determined via a complexometric titration method described by Schwarzenbach and Flaschka [29]. Hydrochloric acid concentration was determined using a TitroLine® autotitrator with 0.1000 M sodium hydroxide as titrant. Calcium 1, 2-cyclohexanediaminetetraacetic acid solution was added to the samples prior to sodium hydroxide titration to prevent interference from copper hydroxide formation. The results from the experiment are reported in Table 5. A potential source of error in this investigation is the oxidation of copper (I) to copper (II) by air. During experimentation, the reactor was monitored for any visual signs of oxidation, including colour changes in the slurry as

well as the development of any blue hue on the cuprous chloride that had deposited on the reactor walls above the liquid level.

Thermodynamic models were produced in this investigation using OLI system software (simulation software for electrolyte chemistry) [30]. The OLI model outputs for the two ternary systems can be used to indicate the feasibility of separating cupric chloride from cuprous chloride. From the comparison in Fig. 12, the cupric chloride solubility is depressed as the hydrochloric acid concentration is increased, until it reaches a minimum, after which it increases again. At the same time, the cuprous chloride solubility continuously increases with a higher hydrochloric acid concentration. These trends yield regions of low cupric chloride solubility and high cuprous chloride solubility. This difference in solubility becomes more pronounced as the temperature decreases. The separation of cuprous from cupric chloride by selective crystallization may be feasible in these regions.

6. Advanced Materials

Studies were conducted to identify and test potential replacement membranes for use in the membrane electrode assembly (MEA) investigated in a previous study [22]. The primary method in this paper to prevent copper crossover is to modify the membrane through polymerization with some promising compounds such as pyrrole and/or aniline. These polymers reduce the porosity of the membrane in such a way that they allow the passage of protons but prevent or reduce other molecules, such as copper cations, to permeate to the cathode area. Such membrane materials have been shown as effective to reduce the rate of methanol crossover in direct methanol fuel cells

(DMFC) [31-34]. The membrane materials that have been shown to have higher selectivity of protons over methanol are expected to also have higher selectivity of protons over Cu species.

6.1 Silane Composite Electrodes

Ceramic carbon electrodes (CCE) were produced through a sol-gel method incorporating a selection of amine containing silanes with increasing numbers of primary and secondary amines. Electrochemical analysis was performed using cell polarization, cyclic voltammetry, and electrochemical impedance spectroscopy. The materials were also characterized with thermogravimetric analysis to assess bulk physical properties. Current electrode technologies rely on a Pt catalyst containing MEA designed for PEM water electrolysis [RW.ERROR - Unable to find reference:595]. Past studies have shown that a platinum catalyst is not required at the anode as the oxidation is occurring at a transition metal centre [36,37]. In aqueous media, Cu(I) will form anionic complexes such as CuCl_2^- or CuCl_3^{2-} . The slow transport of these species to the anode surface severely limits the overall electrochemical reaction. By protonating existing amine groups imparted by the functionalized silanes, there should be an increase in the transport of these anionic species.

Capacitive CV's and EIS were collected in the absence of CuCl to analyze the surface area and ionic conductivity of the different anode materials. These measurements were made in a full-cell MEA configuration constructed from the CCE anode electrode (the test electrode), a Nafion 115 membrane, and a standard Pt-based cathode. Details of these electrochemical measurements are described in detail elsewhere [38, 39]. The CV results indicated that the capacitive surface area

is independent of silane loading (Fig. 13). When normalized for the mass of carbon present on the CCE, the materials showed very similar capacitances. The results showed that the silane loadings between 27-53 wt% had a negligible effect on the surface area of the carbon electrodes. This result was expected since the percentage composition by volume of silane is not significant enough to alter the surface area of the CCE.

The CuCl/HCl electrolysis cell performance was evaluated by plotting current at cell potentials of 0.7 and 1.1 V as a function of anolyte flow rate (Fig. 14). Using this method, the cell response was evaluated to increase the flow at the anode surface. This can also be used to predict the cell's response to higher concentrations of anolyte materials. At 1.1 V, all of the samples showed a linear response to increased flow rate. The 32.4 wt% silane showed the highest performance of all samples. The 27.2 wt% sample showed a steeper response to the increased flow rate meaning that at even higher flow rates, the 27.2 wt% sample may outperform the 32.4 wt% sample. Similar behavior was observed for the 0.7 V comparison. The 32.4 wt% sample also showed the highest current response at 0.7 V. The 27.2 wt% sample showed very comparable currents with a steeper response to the increased flow rates (Fig. 14). While the 27.2 wt% sample showed a slightly lower current response, at higher flow rates or concentrations, the 27.2 wt% sample should perform the best of all tested CCE's.

From the produced silanes, some target composition ranges were identified (Table 6). Silane loading was found to be optimized between approximately 4.8 and 6.8 mmol of silane per gram of carbon in the CCE material. The silane-to-carbon ration (in units of mmol gC^{-1}) value was

found to be consistent across the three silane types tested. Comparing the three materials, it was observed that there is an increase in current response from the CCE samples from the 3-aminopropyl-trimethoxysilane (1N) materials to the 3-trimethoxysilyl-propyl-ethylenediamine (2N) materials, with the 3-trimethoxysilylpropyl-diethylenetriamine (3N) materials showing the best overall performance. Additionally, the 2N and 3N materials showed an increased stability and resistance to copper crossover. The 2N and 3N materials showed limiting currents comparable to or potentially better than those seen in past studies without the use of a Pt catalyst [35,40]. It is important to note that there is a discrepancy between the current responses recorded through potential stair step/LSV and those measured with potentiostatic holds. The increase in the current response from the potential stair step/LSV measurements can be attributed to a preloading of CuCl at the surface of the electrode.

6.2 Nafion/polypyrrole (Ppy) Composite Membranes

Other electrode composites have also been investigated as possible electrode membrane materials. In this section, a series of Nafion/polypyrrole (Ppy) composite membranes (Nafion NRE212, Nafion 115 (N115) (1100 EW) and Nafion 117 (N117)) were fabricated and their selectivity for protons over both Cu and methanol are compared. Proton conductivity was determined via electrochemical impedance spectroscopy (EIS). EIS measurements were taken by applying a 100 mV sinusoidal voltage across the electrodes over a frequency range of 10 MHz to 100 Hz. All EIS data was fitted to the simple equivalent circuit, consisting of the membrane capacitance, connected in parallel to the membrane ionic resistance (R_m) and both connected in

series with a contact resistance. The typical EIS response is a semi-circle Nyquist plot, where the diameter of the semi-circle corresponds to R_m [41-43].

Water contents obtained by Karl Fisher (KF) titration are listed in Table 7. The water content ranges from 6.1 to 16.1 %, for pure Nafion membranes, and from 1.7 to 6.7 % for Nafion pyrrole membranes. In all cases, the presence of Ppy yielded lower water content over the unmodified membrane. This data is in agreement with the TGA data, and also prior reports that observed a decrease in water content that was ascribed to decrease porosity in the composite membranes [32].

The proton conductivities determined from these plots are listed in Table 7. All unmodified membranes displayed proton conductivity values between 0.09 and 0.10 S/cm, which is in agreement with literature values reported for Nafion [44-46]. When composites are formed, there is a significant reduction in proton conductivity in all cases. The largest reduction occurs for NRE 212, which is most likely due to the fact it is the thinnest membrane and likely contains the highest wt % Ppy. The proton conductivities measured in this study are still in a range suitable for full cell applications and in agreement with those reported for Nafion/Ppy composites in DMFC applications [47]. The expected area specific resistances (ASR) for each membrane when assembled in an MEA configuration (i.e. through plane) are listed in Table 7.

Methanol permeability has been measured for the unmodified Nafion membranes and as well the Nafion/Ppy membranes (Table 7). The methanol permeability values measured for Nafion are comparable with those reported in the literature [48]. The values for N115 and N117 are quite

close as expected since the samples are made by the exact same chemical process. NRE 212 has a lower permeability, which can be explained by the presence of capping groups in its structure to promote stability. Each composite shows a significant reduction in methanol permeability over its unmodified counterpart (ca. a 50 – 67 % reduction).

7. System Modeling for Cycle Enhancements

Multi-generation systems are often attractive due to their higher energy and exergy efficiencies than individual cycles (i.e., steam or gas turbine cycles). An increase in efficiency often allows, for the same output, less resources (or exergy) consumed. This section highlights recent studies with multi-generation systems involving the Cu-Cl cycle. Oxygen as a product of the Cu-Cl cycle is also treated as a byproduct, which is sufficiently pure for use or sale [49] in other industrial processes. All the systems also have the capability of providing cooling, hot water and drying air.

A LiBr-H₂O absorption cooling system (ACS) is considered in the study for the multi-generation system, which uses excess energy of solar/nuclear heat transfer fluid to derive a cooling effect. The absorption cooling system is used instead of a conventional cooling system in order to utilize waste heat. Hot water at 42 °C is supplied to a community by the integrated system. Also, drying air for industrial or residential applications is obtained by heating ambient air to the drying temperature (50 °C) using excess heat of the exhaust gases.

Solar thermal energy, concentrated by a heliostat solar tower, is the energy source of System I (Fig. 15). Molten salt (which has a composition of 60 % NaNO₃ and 40 % KNO₃, on a

mass basis) is considered as the heat transfer fluid (HTF) to supply heat to the Cu-Cl cycle. Molten salt has an advantage in that the solar heat can be stored for tens of hours for use at night, or when sunlight is not available [50]. The efficiency of the solar energy and conversion processes are not considered in the present study. Heat is supplied to the copper oxychloride decomposition step (step 4) since this step has the highest temperature heat requirement (530 °C) in the cycle. Heat is also transferred to the hydrolysis step (step 3) of the Cu-Cl cycle and then hydrogen production (step 1) and drying processes (step 2). The temperature of the molten salt is increased to 650 °C, so as to match the heat requirements of the Cu-Cl cycle [50]. The temperature of the molten salt in a low temperature storage tank is higher than 250 °C which is about 30 °C higher than the melting point of the molten salt. A hydrogen storage tank and fuel cell unit are also integrated with the Cu-Cl cycle for energy management. Energy management with a hydrogen storage option is promising, since hydrogen can be converted to electricity efficiently in the fuel cells during peak hours.

System I also comprises a steam turbine cycle, which has a low pressure and high pressure steam turbine, and LiBr-H₂O ACS. The steam turbine cycle and absorption system utilize solar energy. The second Cu-Cl based integrated system utilizes nuclear energy. A Generation IV Supercritical Water Cooled Reactor (SCWR) is a match with the Cu-Cl cycle. The HTF can be either water or molten salt in this case. Unlike solar based systems, the nuclear plant can continuously supply heat to the Cu-Cl cycle using water as the HTF. The coolant (water) inlet and exit temperatures are set as 350 and 625 °C, respectively. Also, the coolant pressure and mass flow

rate are 25 MPa and 1320 kg/s [51]. The LiBr-H₂O ACS is also introduced for cooling, indicating multi-generation of hydrogen, process heat, and cooling from System II. A hydrogen storage and fuel cell unit are also used in System II (Fig. 16).

The energy efficiency of System I can be expressed as follows:

$$\eta_{en} = \frac{\dot{m}_{H_2} \times LHV_{H_2} + \dot{W}_{net} + \dot{Q}_{cooling} + \dot{m}_{air} \times (h_{air} - h_{air,0}) + \dot{m}_{hot\ water} \times (h_{hot\ water} - h_{water,0})}{\dot{m}_{htf} \times (h_1 - h_{12})} \quad (7)$$

where \dot{m} , LHV , \dot{W}_{net} , $\dot{Q}_{cooling}$, and h are the mass flow rate, lower heating value, net work output, refrigeration capacity and specific enthalpy respectively.

The exergy efficiency of System I can be expressed as follows:

$$\eta_{ex} = \frac{\dot{E}x_{H_2} + \dot{W}_{net} + \dot{E}x_{Q_{cooling}} + \dot{m}_{air} \times (ex_{air} - ex_{air,0}) + \dot{m}_{hot\ water} \times (ex_{hot\ water} - ex_{water,0})}{\dot{m}_{htf} \times (ex_1 - ex_{12})} \quad (8)$$

where $\dot{E}x$ and ex are the total and specific exergy of the flow streams. The energy efficiency of System II is given as follows:

$$\eta_{en} = \frac{\dot{m}_{H_2} \times LHV_{H_2} + \dot{Q}_{cooling} + \dot{m}_{air} \times (h_{air} - h_{air,0}) + \dot{m}_{hot\ water} \times (h_{hot\ water} - h_{water,0})}{\dot{m}_{htf} \times (h_1 - h_{12}) + W_{in,CuCl}} \quad (9)$$

where $W_{in,CuCl}$ is the work supplied to the Cu-Cl cycle. The exergy efficiency of System II is:

$$\eta_{ex} = \frac{\dot{E}x_{H_2} + \dot{E}x_{Q_{cooling}} + \dot{m}_{air} \times (ex_{air} - ex_{air,0}) + \dot{m}_{hot\ water} \times (ex_{hot\ water} - ex_{water,0})}{\dot{m}_{htf} \times (ex_1 - ex_{12}) + W_{in,CuCl}} \quad (10)$$

Fig. 17(a) shows the energy and exergy efficiencies of System I and its sub-units. The overall energy efficiency of System I is about 70%, whereas the exergy efficiency is 57%. If the

heat released by the condenser of the steam turbine cycle is not utilized as hot water, the energy efficiency drops to about 51%. The exergy efficiency of the Rankine cycle (STC) is greater than its energy efficiency, since the exergy of heat input is lower than the energy of the heat input.

The energy and exergy efficiencies of System II and its sub-units are shown in Fig. 17(b). The overall energy efficiency of System II is 51 % and the exergy efficiency is 41 %. The absorption cooling system and the Cu-Cl cycle used in System II have similar efficiency values as System I. The energy percentages of all outputs for both systems vary by about 11 % for hydrogen production. The energy percentages of hot water and drying air are 31 % and 14 % for System I and 19 % and 20 % for System II. The exergy percentages, however, are 4 % in total for System I and 3 % in total for System II, since drying air and hot water temperatures are close to the reference temperature, The exergies of power and hydrogen generation have the highest exergy content in System I, 27 % and 64 %, respectively. The exergy of the hydrogen production of System II is about 94 % of total exergy output of the system.

8. Conclusions

Recent advances in the thermochemical Cu-Cl cycle have been presented in this paper. A long-term electrolyzer performance test of more than 1600 h was successfully conducted to demonstrate the promising potential of the electrolyzer for hydrogen production within the Cu-Cl cycle. Experimental and numerical results for mass transfer in multiphase systems involving gas-liquid bubble frequency and solubility of CuCl in HCl solution have been presented. The molten salt reactor design for scaling up the Cu-Cl cycle was also reported.

Decreasing the flow rate of the anolyte in the electrolyzer caused the rate of diffusion of copper (I) through the membrane to decrease. Decreasing the HCl concentration from 11 to 6 M increased the amount of copper (I) that entered the catholyte by a factor of 4. Solubility data for the CuCl-HCl-H₂O ternary system was obtained at 298, 318, 333, 348, and 363 K. A comparison of the OLI model predictions for both the CuCl-HCl-H₂O and CuCl₂-HCl-H₂O ternary systems showed regions where selective precipitation should be feasible. Thermodynamic analyses based on energy and exergy efficiencies were successfully performed to investigate the performance of the Cu-Cl cycle linked with multi-generation systems. The overall energy efficiency of System I is 70 % whereas the exergy efficiency is 57 %. The overall energy efficiency of System II is 51 % and its exergy efficiency is 41 %.**Acknowledgements**

Support of this research from Atomic Energy of Canada Limited, Ontario Research Excellence Fund, Natural Sciences and Engineering Research Council of Canada, University Network of Excellence in Nuclear Engineering (UNENE) and the Canada Research Chairs program are gratefully acknowledged.

References

- [1] Forsberg CW. Future hydrogen markets for large-scale hydrogen production systems. *Int J Hydrogen Energy* 2007; 32:431-9.
- [2] Lewis MA, Masin JG, O'Hare PA. Evaluation of alternative thermochemical cycles, Part I: The methodology. *Int J Hydrogen Energy* 2009; 34: 4115-24.

- [3] Naterer GF, Suppiah S, Lewis MA, Gabriel K, Dincer I, Rosen MA, Fowler M, Rizvi G, Easton EB, Ikeda BM, Kaye MH, Lu L, Pioroi I, Spekkensk P, Tremainel P, Mostaghimim J, Avsecn J, Jiang J. Recent Canadian advances in nuclear-based hydrogen production and the thermochemical Cu–Cl cycle. *Int J Hydrogen Energy* 2009; 34: 2901-17.
- [4] Suppiah S, Stolberg L, Boniface H, Tan G, McMahon S, York S, Zhang W. Canadian nuclear hydrogen R&D programme: Development of the medium-temperature Cu-Cl cycle and contributions to the high-temperature sulphur-iodine cycle. Fourth Information Exchange Meeting, Oakbrook, Illinois, USA, 14-16 April 2009.
- [5] Lewis MA, Ferrandon MS, Tatterson DF, Mathias P. Evaluation of alternative thermochemical cycles–Part III further development of the Cu–Cl cycle. *Int J Hydrogen Energy* 2009; 34: 4136-45.
- [6] Aghahosseini S, Dincer I, Naterer GF. Integrated gasification and Cu–Cl cycle for trigeneration of hydrogen, steam and electricity. *Int J Hydrogen Energy* 2011; 36: 2845-54.
- [7] Rosen MA, Naterer GF, Sadhankar R, Suppiah S. Nuclear-based hydrogen production with a thermochemical copper-chlorine cycle and supercritical water reactor: equipment scale-up and process simulation. *Int J Energ Res* 2012; 36: 456-45.
- [8] Litwin RZ, Pinkowski SM. Solar power for thermochemical production of hydrogen. US Patent Publication US 2008/0256952; Oct 23, 2008.

- [9] Pope K, Naterer GF, Wang Z. Nitrogen carrier gas flow for reduced steam requirements of water splitting in a packed bed hydrolysis reactor. *Exp Therm Fluid Sci* 2012; 44: 815-24.
- [10] Ferrandon MS, Lewis MA, Alvarez F, E. Shafirovich. Hydrolysis of CuCl_2 in the Cu–Cl thermochemical cycle for hydrogen production: Experimental studies using a spray reactor with an ultrasonic atomizer. *Int J Hydrogen Energy* 2010; 35:1895-904.
- [11] Ferrandon MS, Lewis MA, Tatterson DF, Gross A, Doizi D, Croizé L, Dauvois V, Roujou J, Zanella Y, Carles P. Hydrogen production by the Cu–Cl thermochemical cycle: Investigation of the key step of hydrolysing CuCl_2 to Cu_2OCl_2 and HCl using a spray reactor. *Int J Hydrogen Energy* 2010; 35: 992-1000.
- [12] Lewis MA, Masin JG. The evaluation of alternative thermochemical cycles–Part II: The down-selection process. *Int J Hydrogen Energy* 2009; 34:4125-35.
- [13] Daggupati V., Naterer GF, Gabriel K, Gravelins R, Wang Z. Equilibrium conversion in Cu–Cl cycle multiphase processes of hydrogen production. *Thermo Acta* 2009; 496:117-23.
- [14] Marin G, Wang Z, Naterer GF, Gabriel K. Byproducts and reaction pathways for integration of the Cu–Cl cycle of hydrogen production. *Int J Hydrogen Energy* 2011; 36:13414-24.
- [15] Wang Z, Daggupati V, Marin G, Pope K, Xiong Y, Secnik E, Naterer GF, Gabriel K. Towards integration of hydrolysis, decomposition and electrolysis processes of the Cu–Cl thermochemical water splitting cycle. *Int J Hydrogen Energy* 2012; 37:16557-699.

- [16] Aghahosseini S, Dincer I, Naterer GF. Process integration of hydrolysis and electrolysis processes in the Cu–Cl cycle of hydrogen production. *Int J Hydrogen Energy* 2013; 38:9633-43.
- [17] Naterer GF, Suppiah S, Stolberg L, Lewis MA, Ferrandon M, Wang Z, Dincer I, Gabriel K, Rosen M, Secnik E. Clean hydrogen production with the Cu–Cl cycle—progress of international consortium, I: experimental unit operations. *Int J Hydrogen Energy* 2011; 36:15472-85.
- [18] Wang Z, Naterer GF, Gabriel K, Gravelins R, Daggupati V. New Cu-Cl thermochemical cycle for hydrogen production with reduced excess steam requirements. *Int J Green Energy* 2009; 6:616-26.
- [19] Chukwu C, Naterer GF, Rosen MA. Process simulation of nuclear-produced hydrogen with a Cu-Cl cycle. CNS 29th Conference, Toronto, Ontario, Canada, June 1-4, 2008.
- [20] De Micco G, Bohé A, Pasquevich D. A thermogravimetric study of copper chlorination. *J Alloys Compounds* 2007; 437: 351-9.
- [21] Lewis MA, Ahmed S, Lvov S, Fan C. II.E.2 Membrane/Electrolyzer development in the Cu-Cl thermochemical cycle. DOE Hydrogen and Fuel Cells Program, Argonne, IL, 2012.
- [22] Naterer GF, Suppiah S, Stolberg L, Lewis MA, Z. Wang Z, Dincer I, Rosen MA, Gabriel K, Secnik E, Easton EB, Pioro I, Lvov S, Jiang J, Mostaghimi J, Ikeda BM, Rizvi G, Lu L, Odukoya A, Spekkens P, Fowler M, Avsec J. Progress of international hydrogen production network for the thermochemical Cu–Cl cycle. *Int J Hydrogen Energy* 2013; 38: 740-59.

- [23] Schatz R, Kim S, Khurana S, Fedkin M, Lvov SN. High efficiency cucl electrolyzer for Cu-Cl thermochemical cycle. ECS Trans 2013; 50:153-64.
- [24] Khurana S, Hall DM, Schatz RS, Lvov SN. Diagnosis and modeling of the CuCl electrolyzer using electrochemical impedance spectroscopy. ECS Trans 2013; 53:41-50.
- [25] Hall DM, Schatz RS, LaRow EG, Lvov SN. CuCl/HCl electrolyzer kinetics for hydrogen production via Cu-Cl thermochemical cycle. ECS Trans 2013; 58: (in press).
- [26] Oldshue JY. Fluid mixing technology. New York: McGraw-Hill; 1983.
- [27] Luyben LW. Chemical reactor design and control. New Jersey: John Wiley & sons; 2007.
- [28] Himmelsbach W, Houlton D, Ortlieb D, Lovallo M. New advances in agitation technology for exothermic reactions in very large reactors. Chem eng sci 2006; 61(9):3044-52.
- [29] Schwartzenbach G, Flaschka H. Complexometric titrations. London: Methuen; 1969.
- [30] OLI Systems Inc., Simulation software for electrolyte chemistry, Accessed March 4, 2013 <http://www.olisystems.com/>.
- [31] Langsdorf BL, Sultan J, Pickup PG. Partitioning and polymerization of pyrrole into perfluorosulfonate (Nafion) membranes under neutral conditions. J Phy Chem B 2003; 107: 8412-15.

- [32] Langsdorf BL, MacLean BJ, Halfyard JE, Hughes JA, Pickup PG. Partitioning and polymerization of pyrrole into perfluorosulfonic acid (Nafion) membranes. *J Phy Chem B* 2003; 107:2480-84.
- [33] Xu F, Innocent C, Bonnet B, Jones D, Roziere J. Chemical modification of perfluorosulfonated membranes with pyrrole for fuel cell application: preparation, characterisation and methanol transport. *Fuel Cells* 2005; 5:398-405.
- [34] Neburchilov V, Martin J, Wang H, Zhang J. A review of polymer electrolyte membranes for direct methanol fuel cells. *J Power Sources* 2007; 169:221-38.
- [35] Kim S, Schatz RS, Khurana K, Fedkin MV, Wang C, Lvov SN. Advanced CuCl electrolyzer for hydrogen Pproduction via the Cu-Cl thermochemical Cycle. *ECS Trans* 2011; 35: 257-65.
- [36] Ranganathan S, Easton EB. Ceramic carbon electrode-based anodes for use in the Cu-Cl thermochemical cycle. *Int J Hydrogen Energy* 2010; 35:4871-6.
- [37] Ranganathan S, Easton EB, High performance ceramic carbon electrode-based anodes for use in the Cu-Cl thermochemical cycle for hydrogen production, *Int J Hydrogen Energy* 2010; 35: 1001-7.
- [38] Ranganathan S, Edge PS, Easton EB. Evaluation of anode electrode materials for Cu-Cl/HCl electrolyzers for hydrogen production. *ECS Trans* 2012; 41:111-20.

- [39] Edge PSR, Easton EB, Comparison of novel anode materials for the production of hydrogen using CuCl/HCl electrolyzers. *ECS Trans* 2013; 53:11-20.
- [40] Balashov VN, Schatz RS, Chalkova E, Akinfiyev NN, Fedkin MV, Lvov SN. CuCl electrolysis for hydrogen production in the Cu–Cl thermochemical cycle. *J Electrochem Soc* 2011; 158:B266-75.
- [41] Peckham TJ, Schmeisser J, Holdcroft S. Relationships of acid and water content to proton transport in statistically sulfonated proton exchange membranes: variation of water content via control of relative humidity. *J Phy Chem B* 2008; 112:2848-58.
- [42] De Almeida NE, Easton EB. Nafion/sulfonated silica composite membranes for PEM fuel cells. *ECS Trans* 2010; 28: 29-38.
- [43] Nam S, Kim S, Kang Y, Lee JW, Lee K. Preparation of Nafion/sulfonated poly (phenylsilsesquioxane) nanocomposite as high temperature proton exchange membranes. *J Membr Sci* 2008; 322:466-74.
- [44] Rodgers MP, Shi Z, Holdcroft S. Transport properties of composite membranes containing silicon dioxide and Nafion[®]. *J Membr Sci* 2008; 325:346-56.
- [45] Kim J, Kim S, Nam K, Kim D. Composite proton conducting membranes based on Nafion and sulfonated SiO nanoparticles. *J Membr Sci* 2012; 415:696-701.

- [46] Peighambardoust S, Rowshanzamir S, Amjadi M. Review of the proton exchange membranes for fuel cell applications. *Int J Hydrogen Energy* 2010; 35:9349-84.
- [47] Easton EB, Langsdorf BL, Hughes JA, Sultan J, Qi Z, Kaufman A, Pickup PG. Characteristics of polypyrrole/nafiction composite membranes in a direct methanol fuel cell. *J Electrochem Soc* 2003; 150: C735-39.
- [48] Elabd YA, Napadensky E, Sloan JM, Crawford DM, Walker CW. Triblock copolymer ionomer membranes: part I. methanol and proton transport. *J Membr Sci* 2003; 217:227-42.
- [49] Naterer GF, Fowler M, Cotton J, Gabriel KS. Synergistic roles of off-peak electrolysis and thermochemical production of hydrogen from nuclear energy in Canada. *Int J Hydrogen Energy* 2008; 33:6849-57.
- [50] Wang Z, Naterer GF, Gabriel KS, Secnik E, Gravelins R, Daggupati V. Thermal design of a solar hydrogen plant with a copper–chlorine cycle and molten salt energy storage. *Int J Hydrogen Energy* 2011; 36:11258-72.
- [51] Pioro IL, Duffey RB. Heat transfer and hydraulic resistance at supercritical pressures in power engineering applications. New York: ASME Press; 2007, pp.99-135.

List of Figures

Fig. 1: Schematic of the thermochemical copper-chlorine cycle

Fig. 2: Polarization curve for each cell in the 5-cell stack Conditions: Membrane Nafion® 112, Catalyst loading 0.5 mg/cm², Anolyte 1 M CuCl in 7 M HCl, Catholyte 7 M HCl , Flow rate 600 mL/min, 60 °C, 1 bar

Fig. 3: Polarization curves for 4 temperatures Conditions: Membrane Single Pressed Nafion® 117, Catalyst on each electrode: 20% Pt on XC-72R 4 mg/cm², Catalyst loading 0.8 mg/cm², Pressure 1-1.3 bar, Anolyte 2 M CuCl in 7 M HCl, Catholyte 7 M HCl , Flow rate

Fig. 4: Current density (right) and internal ohmic resistance (left) during the 168 hour lifetime test Conditions: Membrane Single Pressed Nafion® 117, Catalyst on each electrode 20% Pt on XC-72R 4 mg/cm², Catalyst loading 0.8 mg/cm² Pt , Anolyte 1-2 M CuCl

Fig. 5: Two SEM images comparing catalyst application differences between painted (left) and airbrushed (right) electrodes

Fig. 6: Cell performance experiment. Anolyte: 0.5 M CuCl in 11 M HCl; catholyte: 11 M HCl, flow rate of 0.6 L•min⁻¹, current density of 0.1 A•cm²

Fig. 7: Crystallization effectiveness for 1 mol of CuCl₂ with input of 2 mol CuCl and 6 mol HCl

Fig. 8: Minimum energy input of hydrolysis reactor

Fig. 9: Excess water with reaction extent per mol of CuCl₂

Fig. 10: (a) Dissolution rate of solid copper (I) chloride in 12M hydrochloric acid; (b) dissolution rate of solid copper (I) chloride in 12M hydrochloric acid in the presence of nitrogen

Fig. 11: Schematic of solubility experimental apparatus for binary and ternary systems

Fig. 12: Comparison between cuprous chloride and cupric chloride solubilities in hydrochloric acid at 298 K, 323 K and 348 K

Fig. 13: CVs obtained for CCE materials with varied 1N silane loading. Measurements were made in the full cell configuration using N₂-purged 2M HCl as the anolyte (working electrode) and flowing hydrogen at the cathode (reference and counter electrode) at a sweep rate of 10 mV/s. Data is shown with current normalized for (a) geometric surface area and for (b) mass of carbon.

Fig. 14: Variation in current densities obtained with anolyte flow rates during CuCl/HCl electrolysis using for CCE anodes containing different amounts of 1N silane at cell potentials of (a) 1.1 V and (b) 0.7 V. Measurements were made at 25 °C with 0.2M CuCl in 2M HCl flowing at the anode, and pure water flowing at the cathode

Fig. 15: Schematic diagram of System I

Fig. 16: Schematic diagram of System II

Fig. 17: Energy and exergy efficiency of (a) System I and (b) System II

Institution	Study Objectives	Active Area (cm ²)	Temperature, °C	HCl concentration, M
AECL	Long term CuCl/HCl cell performance studies	5	45	11 M
AECL	Copper (I) diffusion studies	25	45	11 M
GTI	Scale-up Increase to 5-cell stack	300	60	6-7
GTI	Membrane	6.45	60	6-7
PSU	Effect of temperature	5	40-100	6-7

PSU	Lifetime	5	80	6-7
PSU	Pt loading	5	80	6-7

Table 1: Summary of ongoing work at AECL, GTI and PSU and conditions of the tests

Anolyte	0.5 M CuCl in 11 M HCl
Anode	Catalyst free Graphite

Cathode	Pt Electrocatalyst
Membrane	Nafion® N1110
Current Density	0.1 A/cm ²
Temperature	45°C
Catholyte	11 M HCl
Catholyte Flow Rate	0.6 L/min
Anolyte Flow Rate	0.6 L/min
Electrode Area	5 cm ²

Table 2: Experimental conditions during long term CuCl/HCl electrolysis experiments

Residence Time (h)	H₂ (ton/day)	O₂ (ton/day)	D(m) × H(m) × N
2	100,000	800,000	4.14 × 8.29 × 2
	50,000	400,000	4.14 × 8.29 × 1
	25,000	200,000	3.29 × 6.58 × 1
1	100,000	800,000	4.14 × 8.29 × 1
	50,000	400,000	3.29 × 6.58 × 1
	25,000	200,000	2.61 × 5.22 × 1
0.5	100,000	800,000	3.29 × 6.58 × 1
	50,000	400,000	2.61 × 5.22 × 1
	25,000	200,000	2.07 × 4.14 × 1

Table 3: Dimensions and numbers of oxygen reactors (neglecting bubble volume) for different hydrogen production rates and different residence times

T [°C]	Saturated solution for 1 litre of solution [mol]			Saturated solution for 1 litre of solution normalized to a constant quantity of HCl [mol]		
	CuCl	CuCl ₂	HCl	CuCl	CuCl ₂	HCl
20	1.46	2.31	8.66	1.03	1.63	6.09
40	1.68	3.06	9.73	1.05	1.92	6.09
60	2.08	3.26	8.55	1.48	2.32	6.09
80	1.48	2.82	6.09	1.48	2.82	6.09

Table 4: Crystallization properties

298 K		318 K		333 K		348 K		363 K	
<i>HCl</i>	<i>CuCl</i>								
(mol/kg)	(mol/kg)								
1.2820	0.1175	1.0811	0.1379	1.0867	0.2043	1.3302	0.3350	1.3622	0.4463
3.7856	0.6702	3.8032	0.9109	3.8076	1.0734	3.8083	1.3181	3.9267	1.6366
6.1608	1.5819	6.2678	1.9905	6.3385	2.2578	6.4787	2.6679	7.2798	3.5526
7.1370	1.9815	7.1568	2.4272	7.0652	2.6135	7.1835	3.1121	9.5042	4.5744
10.0924	3.0516	10.3550	3.7892	10.2655	4.0062	10.1334	4.4491	11.3487	5.4435
11.7939	3.7330	10.9241	4.0662	11.8436	4.7969	11.9511	5.2175		

Table 5: Cuprous chloride solubility in hydrochloric acid at temperatures from 298 K to 363 K

Sample Code	wt% Silane	Mass Loading (mg/cm²)	Carbon Loading (mg/cm²)	mMol Si/g_c
B1P73S2	27.1790	1.78	1.2962	3.3930
B1P69S1	32.4223	2.66	1.7976	4.3616
B1P69S2	50.7222	2.79	1.3749	9.3574
B1P69S3	53.4536	3.65	1.6989	10.4399
B1P60S2	62.4869	4.24	1.5906	15.1431

Table 6: 3-Aminopropyl-trimethoxysilane (1N) full cell CCE sample information

Membrane	loss % at 200 °C (TGA)	wt% at 900 °C (TGA)	% H₂O KF	σ_{H^+} S/cm	ASR Ωcm^2	P_{MeOH} $\times 10^6 \text{ cm}^2/\text{s}$	P_{Cu} $\times 10^6 \text{ cm}^2/\text{s}$
NRE212	14.02	0.02	6.44	0.1026	0.0495	0.953	0.637
NRE212/Ppy	5.75	6.124	4.17	0.0133	0.382	0.361	n/a
N115	8.67	0.03	6.12	0.0905	0.140	1.520	0.686
N115/Ppy	6.53	7.22	1.70	0.0149	0.852	0.557	n/a
N117	14.63	0.00	16.05	0.0973	0.188	1.693	1.05
N117/Ppy	8.58	5.74	6.68	0.0330	0.555	0.847	n/a

Table 7: Summary of membrane physical properties (ASR = area specific resistance)

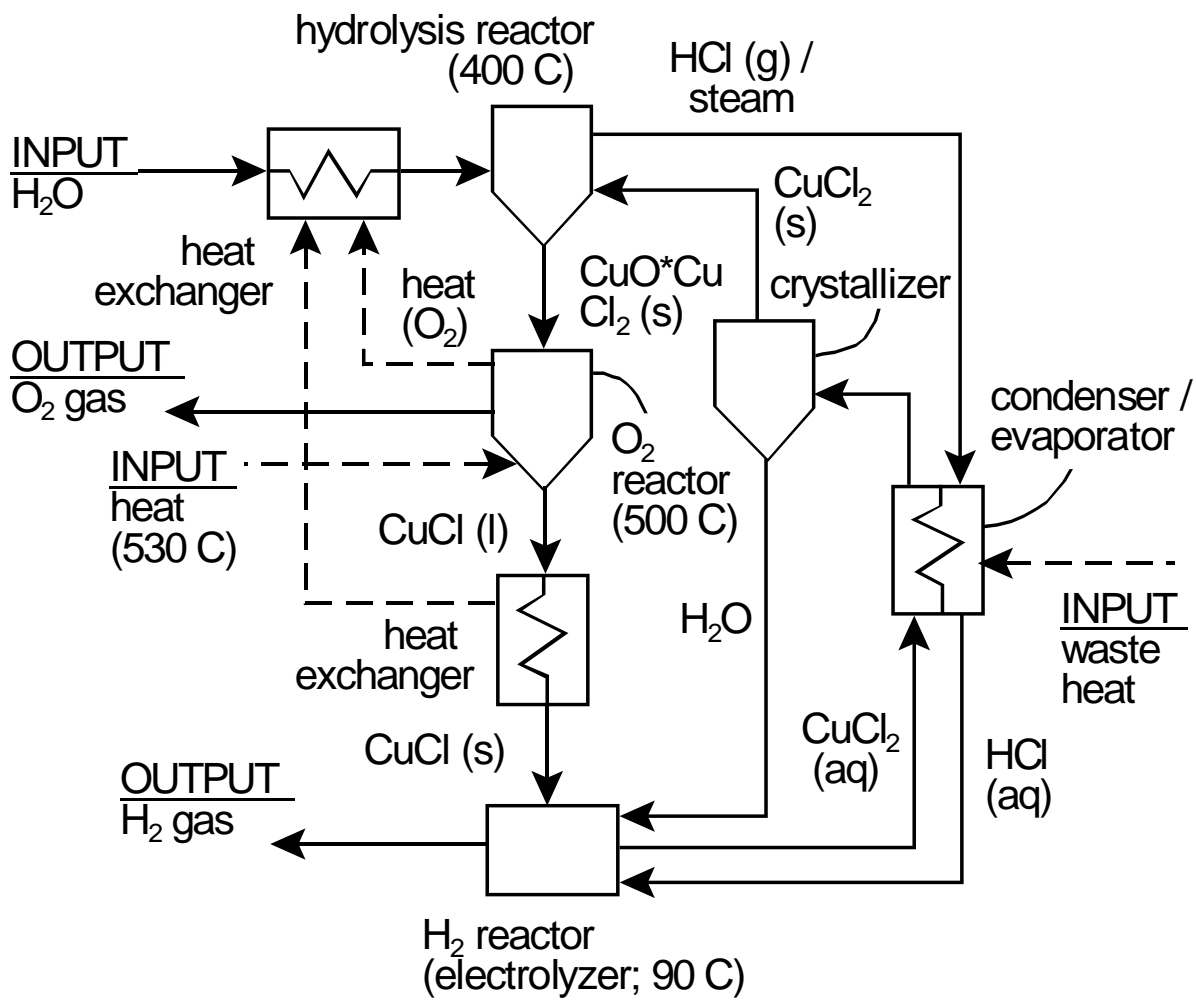


Fig. 1

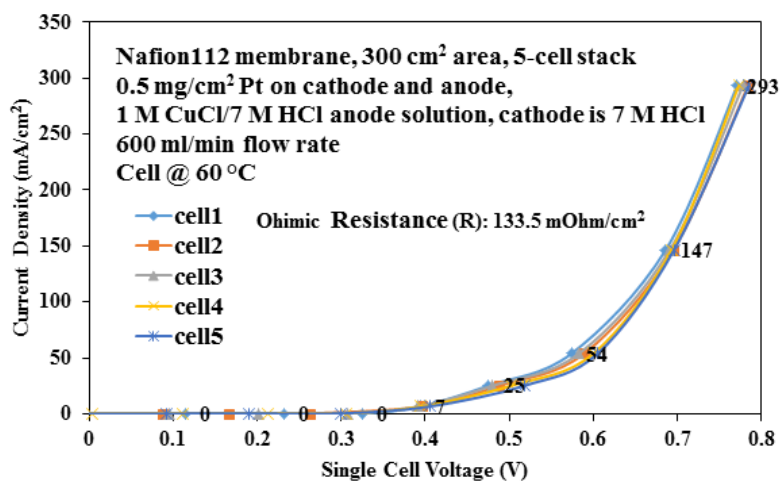


Fig. 2

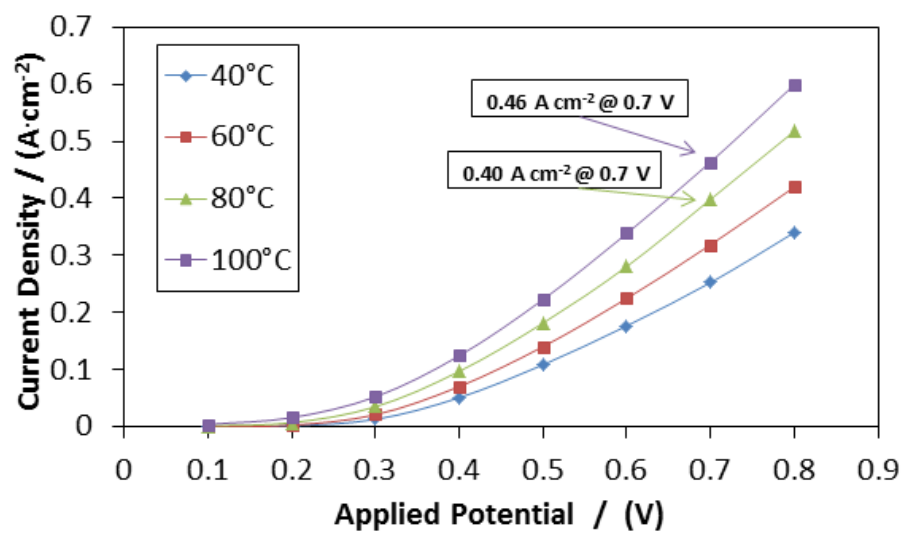


Fig. 3

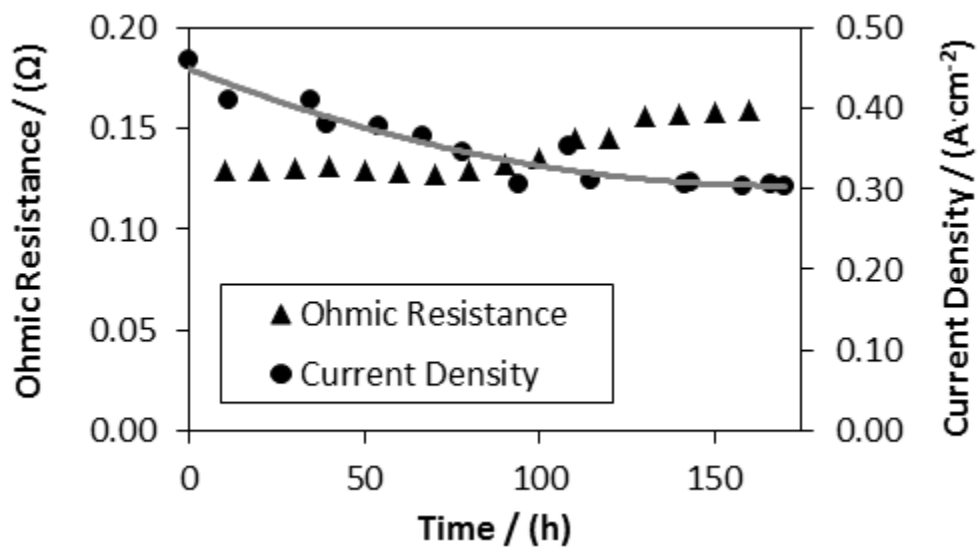


Fig. 4

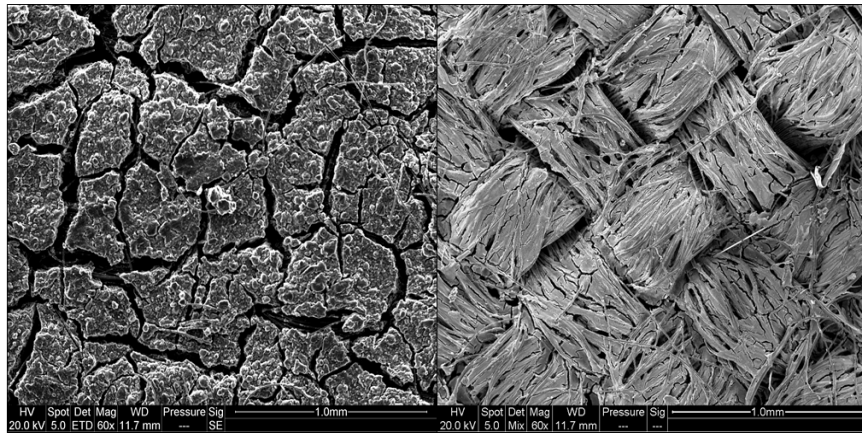


Fig. 5

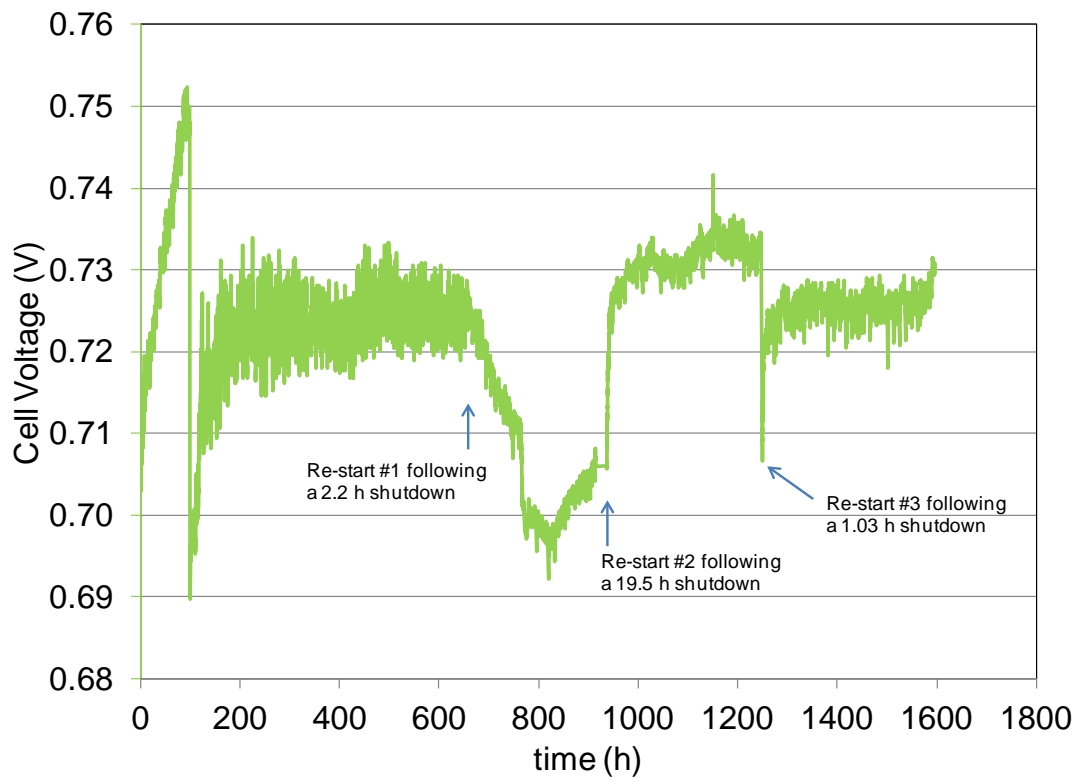


Fig. 6

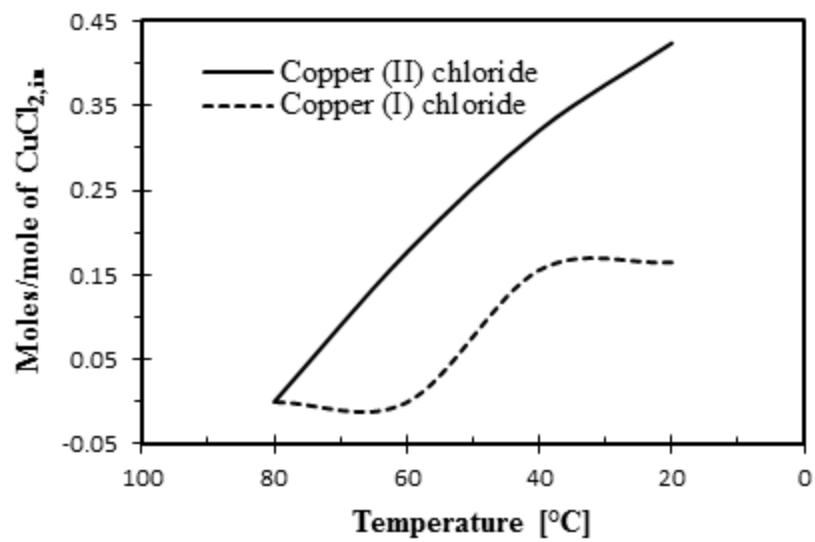


Fig. 7

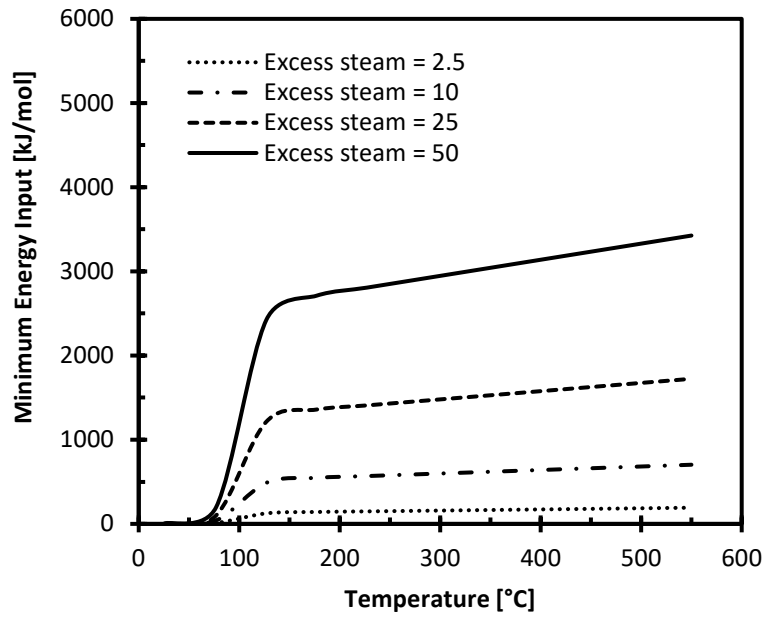


Fig. 8

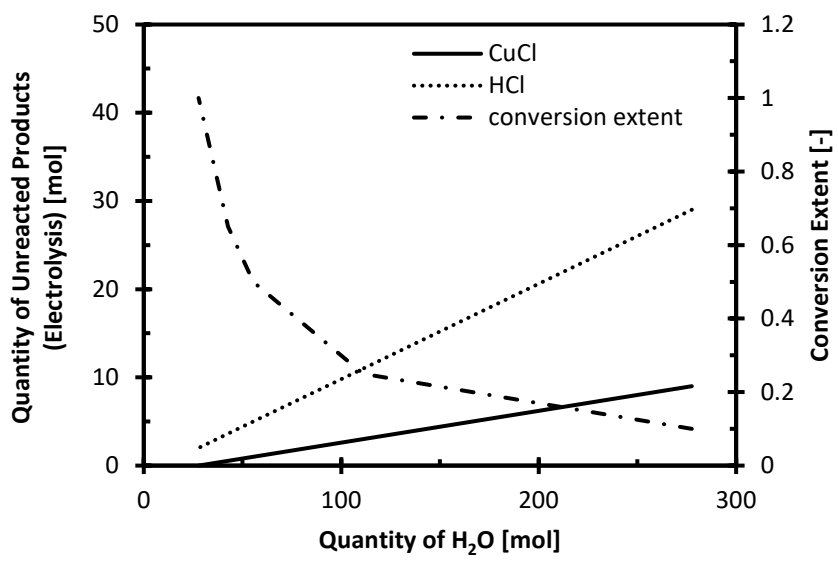
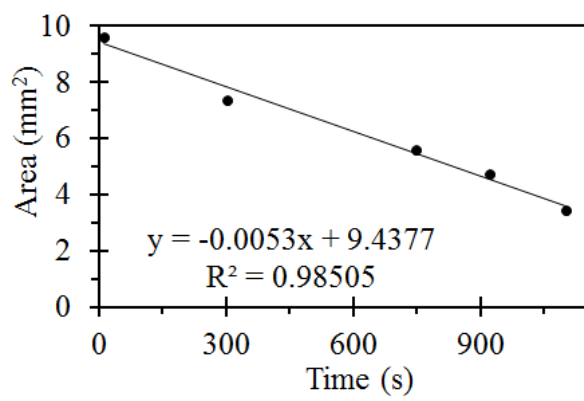
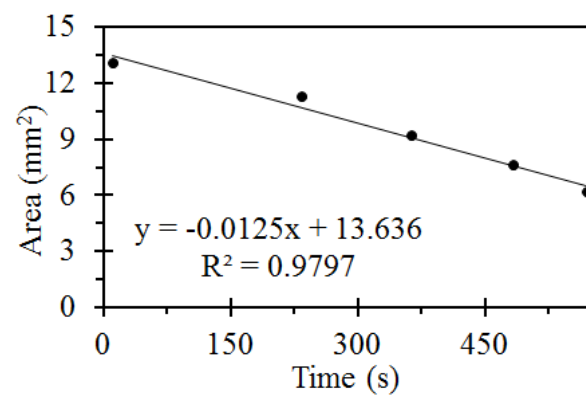


Fig. 9



(a)



(b)

Fig. 10

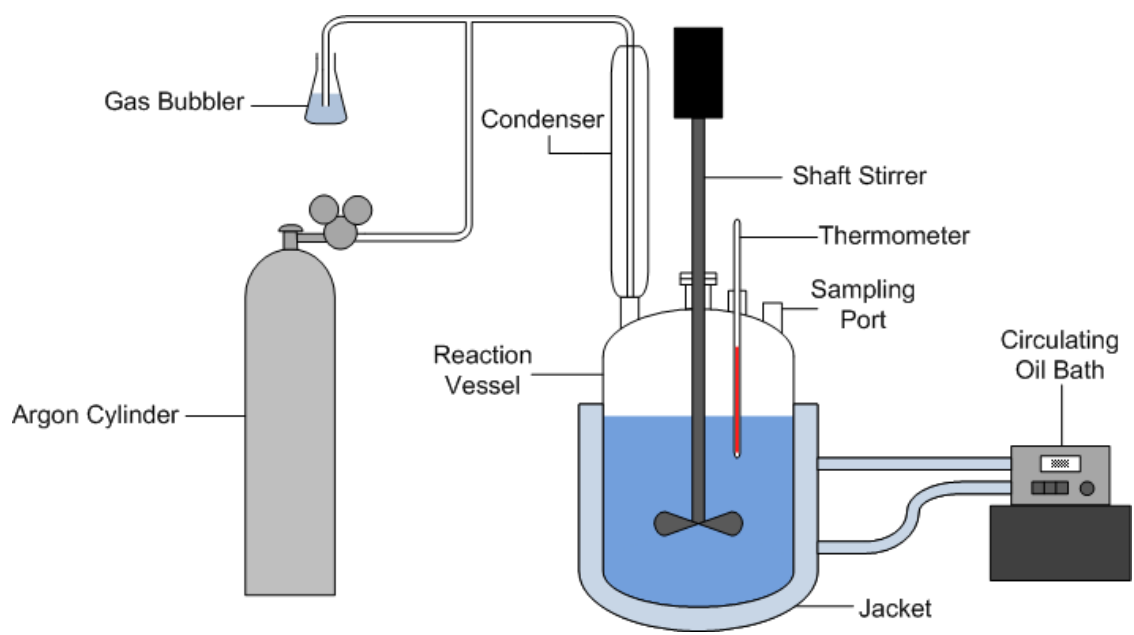


Fig. 11

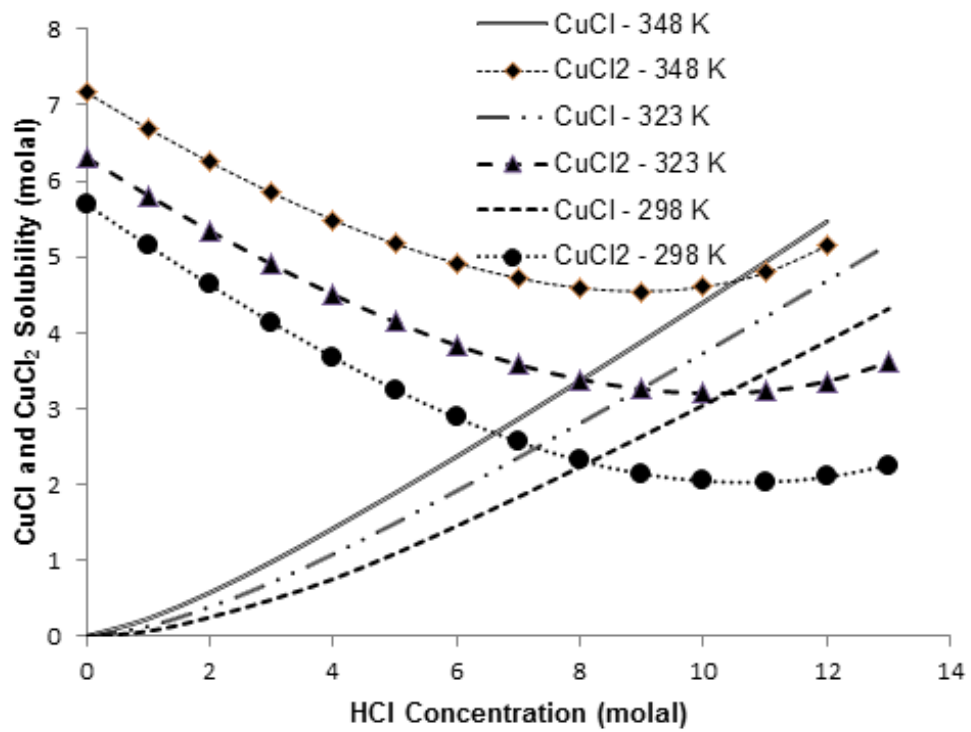


Fig. 12

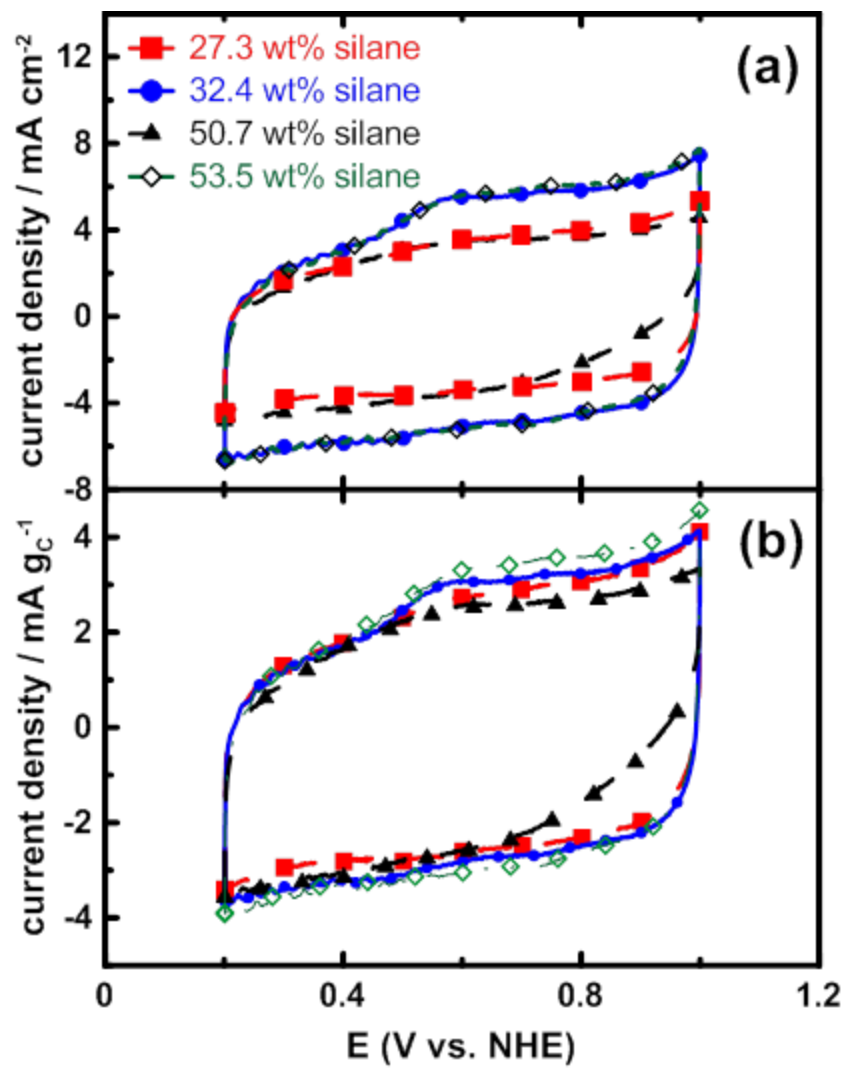


Fig. 13

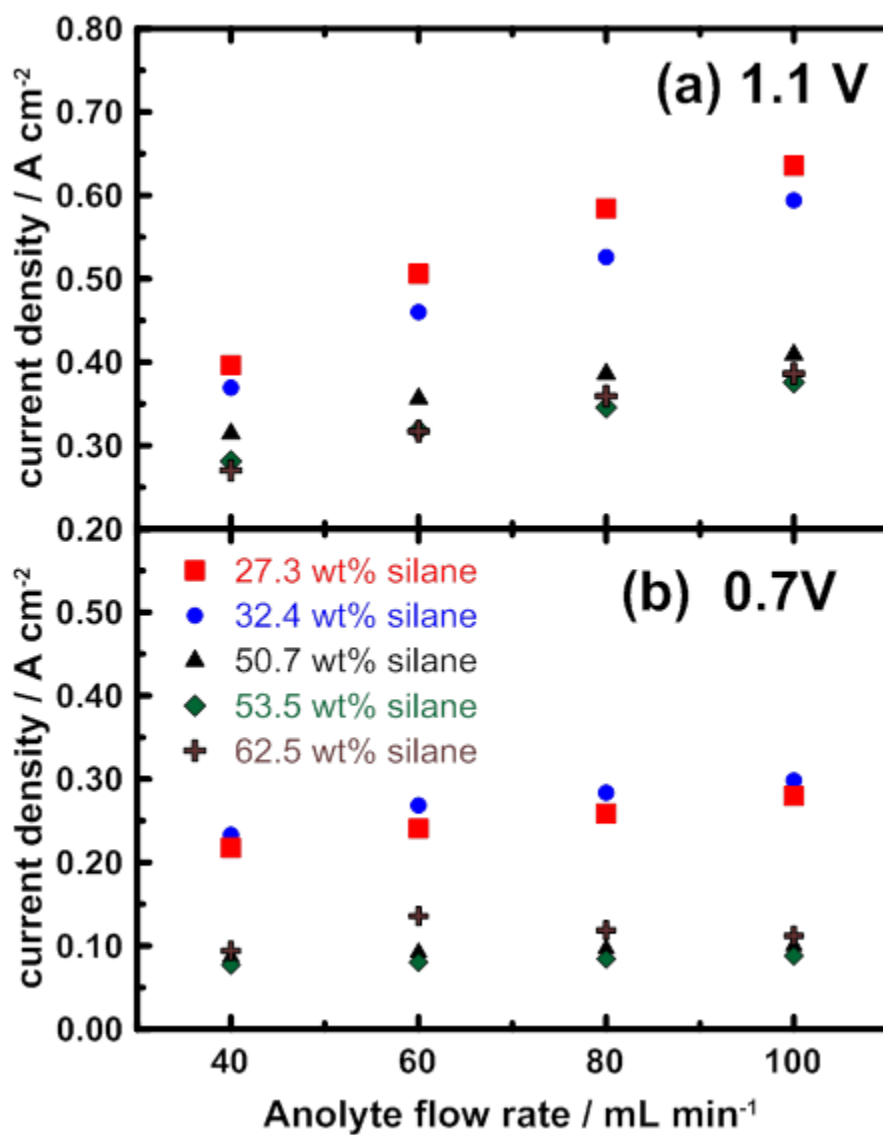


Fig. 14

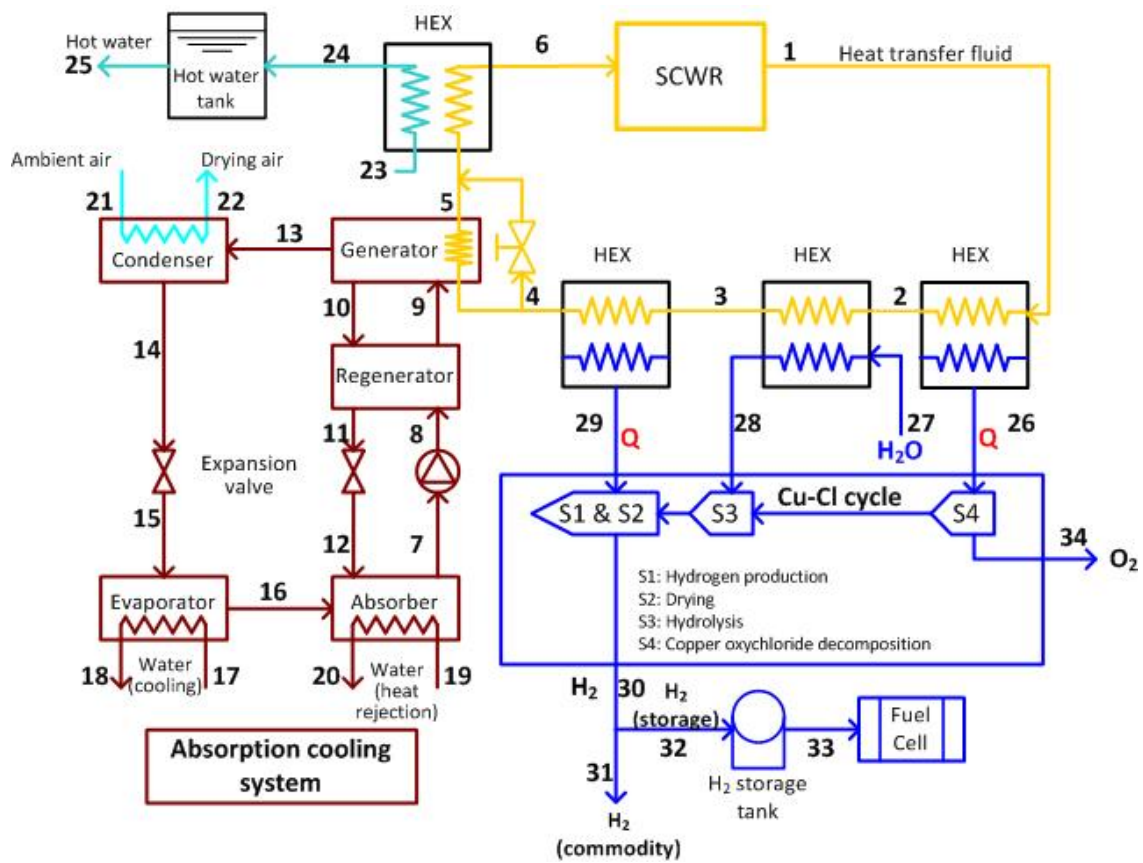
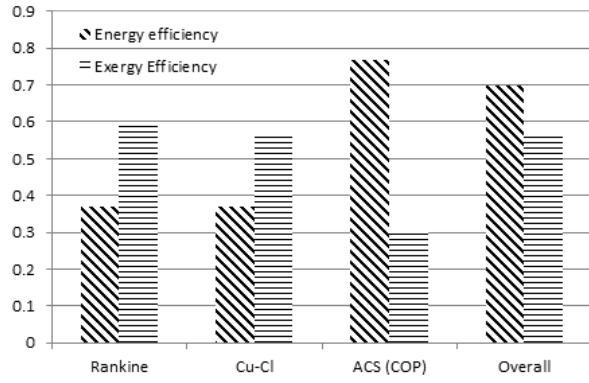
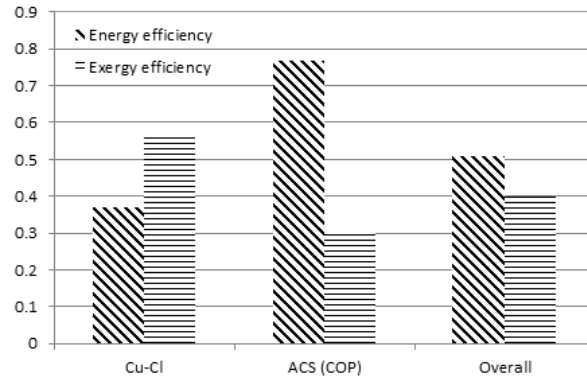


Fig. 16



(a) Energy and exergy efficiency of System I and its sub-units



(b) Energy and exergy efficiency of System II and its sub-units.

Fig. 17